Atomistically informed irradiation induced hardening model for zirconium

P. Noirot, L.M. Dupuy, J. Daubin, Frédéric Mompiou, F. Onimus

Journal of Nuclear Materials 624 (2026) 156480

Contents lists available at ScienceDirect

Journal of Nuclear Materials

journal homepage: www.elsevier.com/locate/jnucmat

Atomistically informed irradiation induced hardening model for zirconium

P. Noirot [a,b], L. M. Dupuy [a], J. Daubin [c], F. Mompiou [d,b], F. Onimus [a,*]

[a] Université Paris-Saclay, CEA, Service de Recherche en Matériaux et procédés Avancés, F-91191, Gif-sur-Yvette, France
[b] Université de Toulouse, UPS, F-31055, Toulouse, France
[c] Université Paris-Saclay, CEA, Service de Génie Logiciel pour la Simulation, F-91191, Gif-sur-Yvette, France
[d] Centre d'Elaboration de Matériaux et d'Etudes Structurales, CNRS UPR 8011, 29 rue J. Marvig, BP 94347, cedex 4 31055, Toulouse, France

ARTICLE INFO

Keywords:
Molecular dynamics
Dislocations dynamics
Irradiation
Dislocation loop
Helical turn
Hardening
Zirconium

ABSTRACT

Neutron irradiation of zirconium alloys leads to the formation of dislocation loops. Their interactions with gliding dislocations are responsible for hardening. Multi-scale numerical simulations of interactions between dislocations and loops are undertaken to predict the mechanical properties evolution of these materials due to irradiation and during post-irradiation annealing. The effect of loop size and density on the resulting hardening is systematically investigated using molecular dynamics simulations. Dislocation dynamics simulations, originally calibrated on molecular dynamics simulations, are used to extrapolate the results to larger loop and box sizes. It is shown that the larger the loop the higher the hardening. An analytical hardening model, originally based on dislocation and precipitate interactions, is proposed. It is able to reproduce very well the hardening induced by loops in a wide range of loop size and density.

1. Introduction

Zirconium alloys are used as fuel cladding tubes for water-cooled nuclear reactors. During in-reactor operation, these materials are subjected to fast neutron irradiation which induces significant changes in the mechanical properties such as hardening. At the microscopic scale, neutron irradiation creates a high density of small point defect clusters, in the form of dislocation loops, that act as obstacles against dislocation glide, thus explaining the hardening [1–5].

After in reactor use, the nuclear fuel assembly is stored in water and is eventually transported, in a dry cask, to a long-term storage facility or to a reprocessing plant. During transportation in dry environment the fuel rod temperature increases due to the residual power of the fuel. This leads to annealing of the cladding tubes made of zirconium alloys resulting in the recovery of the radiation induced hardening. At the microscopic scale, during annealing, the loop density decreases and the mean loop diameter increases [1,6–11].

In order to predict the hardening induced by irradiation and during post-irradiation annealing it is important to develop an analytical physically based model that takes into account the evolution of both loop density and diameter. The best way to do this is to use atomistic simulations [12,13]. Atomistic simulations are however computationally demanding and are limited to small box sizes. This means that only small loop sizes and high loop densities, due to the periodic boundary conditions used, are accessible to this technique. In order to assess the hardening induced by low loop density and large loop size, a mesoscale approach, using discrete dislocation dynamics (DD) simulations [14], can be employed to bridge the length scales. This atomistically-informed multiscale approach should then enable the development of a reliable analytical physically based model.

For several decades, dislocation and loop interactions have been studied using Molecular Dynamics (MD) simulations for various metals with face centered cubic, body-centered cubic or hexagonal close packed (hcp) crystallographic structures [15–24]. The critical stress needed to overcome the obstacle was computed for specific configurations, with given loop size and density. It was shown that the strongest interaction is the interaction between a screw dislocation and a loop. This interaction creates an helical turn on the dislocation which impedes dislocation glide. Overcoming this obstacle requires the closing of the helical turn.

In the case of zirconium, the easy slip system is the prismatic system, with $\langle a \rangle$ Burgers vector in the hcp lattice [25,26]. Furthermore, in zirconium, irradiation mostly creates loops with $\langle a \rangle$ Burgers vector and habit planes close to the prismatic planes. Therefore the interaction which is largely responsible for the hardening is the interaction between a $\langle a \rangle$ screw dislocation gliding in the prismatic plane and a loop with a $\langle a \rangle$ Burgers vector. This is precisely one of the interactions that has been studied by several authors using both MD [23] and DD [27] simulations.

Recently [24], a thorough work has been conducted to parameterize as accurately as possible a DD model on MD simulations for zirconium. Elasticity, dislocation line energy, dislocation mobility and cross-slip

* Corresponding author.
E-mail address: fabien.onimus@cea.fr (F. Onimus).

https://doi.org/10.1016/j.jnucmat.2026.156480
Received 10 October 2025; Received in revised form 14 January 2026; Accepted 25 January 2026
Available online 28 January 2026

parameters were adjusted for a $\langle a \rangle$ dislocation gliding in the prismatic plane. Dislocation-loop interactions, for only one loop size and one loop density (related to the box size) were then simulated by MD and successfully reproduced by DD simulations.

In this paper, we have extended this previous work to determine the effect of loop size and density on the hardening. With this objective, we have undertaken a multi-scale study, using, first, extensive MD simulations for many loop and box sizes. Then, using the adjusted DD model [24], DD simulations were conducted and compared to MD simulations. Once the DD model was validated, it has been used with confidence to extrapolate the results to larger loop sizes and lower loop densities. Finally, we have proposed an analytical model able to describe accurately the hardening induced by irradiation over a wide range of loop sizes and densities.

2. Methods

Similar to our previous study [24], we have employed both MD and DD simulations. While the former are typically used to simulate atomic-scale mechanisms over volumes on the order of tens of nanometers and timescales of a few nanoseconds, the latter are more commonly applied to volumes on the order of micrometers and timescales of milliseconds. The novelty of our study lies in comparing these two techniques at the same spatial and temporal scales.

2.1. Molecular dynamics simulations

2.1.1. General information

The open-source MD code LAMMPS [28] has been employed to perform MD simulations. The MA07#3 EAM inter-atomic potential developed by Mendelev and Ackland [29] was selected. All simulations were conducted at 300 K using a time step of 5 fs. More details concerning the MD simulation procedure can be found in [24].

2.1.2. MD simulation box

The simulation box used in this study is the same as the one used in [24]. The $\hat{\mathbf{x}}$, $\hat{\mathbf{y}}$ and $\hat{\mathbf{z}}$ unit-vectors of the orthogonal simulation box are respectively oriented along the Miller-Bravais directions $[11\bar{2}0]$, $[0001]$, and $[1\bar{1}00]$, as shown in Fig. 1. The corresponding box sizes are respectively L_x, L_y and L_z. Periodic boundary conditions are applied along the $\hat{\mathbf{x}}$ and $\hat{\mathbf{y}}$ directions. The box is divided into three main regions along the $\hat{\mathbf{z}}$ direction: bottom (fixed), middle (mobile) and top with relative atomic positions kept fixed. As discussed in Section 2.1.4, this slicing is used to apply appropriate mechanical loading on the simulation box. The thickness (e) of the top and bottom regions is equal to 0.96 nm *i.e.* larger than the potential cutoff value of 0.76 nm. In this box a screw dislocation with a $\frac{1}{3}[11\bar{2}0]$ Burgers vector and gliding in the $(1\bar{1}00)$ prismatic plane is introduced. Furthermore, a nearly square interstitial dislocation loop with the same Burgers vector $\frac{1}{3}[11\bar{2}0]$ is also introduced in front of the dislocation. The center of the square loop is located on the dislocation glide plane. The procedure to introduce both loop and dislocation is described in [24]. It should be pointed out that in the following study the Burgers vector of the loop is always the same. The interaction between the dislocation and the loops with the two other $\langle a \rangle$ Burgers vectors, that are different from the Burgers of the dislocation, are not considered. This is justified by the fact that for all three different configurations, the same helical turn is formed, resulting ultimately in the same interaction and thus same critical stress [24,30].

2.1.3. Loop size and loop density

In this study, nearly-square loops have been introduced with a given number ($n = m^2$) of self interstitial atoms (SIA), where m is the number of SIAs along each side. The size of the loop in the basal plane is $l_{\text{basal}} = \frac{c}{2}m$ and the size of the loop in the prismatic plane is $l_{\text{prismatic}} = \frac{a\sqrt{3}}{2}m$, where a and c are the lattice parameters of the α-Zr (hcp) with $a = 0.323$ nm and $c = 0.5176$ nm. Real loops being circular, we chose to define the equivalent size D, as the diameter of a circle having the same area as the actual loop, therefore

$$D = \sqrt{ac\sqrt{3} \times \frac{n}{\pi}}$$

Our calculation setup amounts to an infinite periodic row of prismatic loops with an inter-loop distance L_x along the screw dislocation line through the use of periodic boundary conditions, which is obviously a simplification of actual configurations. It is nevertheless interesting to define the corresponding equivalent loop density N (number of loops per unit volume) such that the average loop inter-spacing in the dislocation glide plane ($L_x = 1/\sqrt{N\,D}$) is equal to L_x. Using this definition, the loop density is equal to $N = 1/(DL_x^2)$. The results obtained for a box size L_x are then associated with the behaviour of the actual material with a loop density N with diameter D (Fig. 2), the different values of L_x and D being chosen independently.

2.1.4. Mechanical loading

Following previous similar studies (e.g. [12]), shear strain is applied at a constant rate $\dot{\gamma}_{xz}^{\text{MD}} = 1 \times 10^7\ \text{s}^{-1}$ by assigning a constant velocity $\hat{v} = (\dot{\gamma}_{xz}^{\text{MD}} L'_z, 0, 0)$ to the top regions, whereas atoms in the bottom region are held at fixed positions. Note that only the height $L'_z = L_z - 2e$ of the middle (mobile) region is considered. Hence, dislocations move at an average velocity given by equation:

$$v = \frac{L_y L'_z \dot{\gamma}_{xz}^{\text{MD}}}{b}, \tag{1}$$

where b is the Burgers vector length of $\langle a \rangle$ dislocations ($b = a$). This leads to a dislocation velocity equal to $29.8\ \text{m s}^{-1}$ as in the study done by Serra and Bacon [23].

2.2. Dislocation dynamics simulations

2.2.1. The DD code NUMODIS

Numerical DD simulations were performed using the code NUMODIS developed at CEA in collaboration with Grenoble INP, CNRS and INRIA. The dislocation lines are represented as a set of nodes connected by linear segments. A Burgers vector and a glide plane are attributed to each segment. Contrary to segment based codes [31,32], the nodes are free to move in the dislocation glide plane and are not attached to a discrete grid. The NUMODIS code bears some similarities with other codes such as the Karlsruhe code [33] or ParaDis [34,35]. More details on this numerical code can be found in [24].

2.2.2. DD parameters

The DD code NUMODIS requires the introduction of several parameters, such as the lattice parameters, the isotropic elasticity coefficients, dislocation line energy and dislocation mobility coefficients. All these parameters have been deduced from MD simulations thanks to a thorough study described in details in [24]. The cross-slip mechanism from basal to prismatic slip system has been taken into account by introducing a test angle θ_{detect} between the dislocation segment and the screw orientation. During the simulation, the angle between the dislocation line in the basal plane and the screw direction is measured for each segment (θ). If this angle (θ) is below θ_{detect}, then segment is forced to align along the screw direction and is now able to glide in the prismatic plane. If the segment is not stable in the prismatic plane, cross-slip does not occur and the segment remains in the basal plane.

The discretization lengths ($l_{\min} = 0.6$ nm and $l_{\max} = 2.4$ nm) were chosen in order to ensure an adequate representation of the loop sides, while maintaining the minimal length above the Burgers vector length b. The time step chosen is equal to 1×10^{-5} ns.

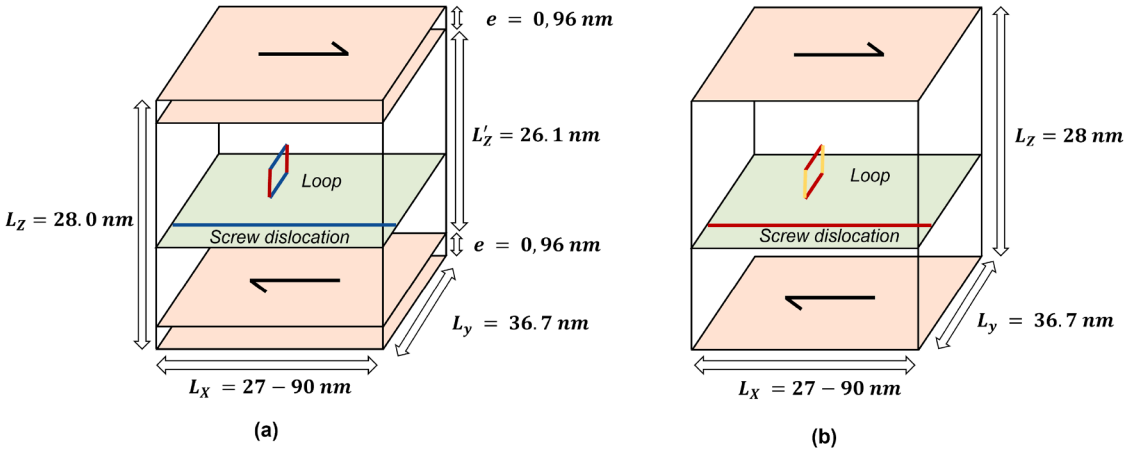

Fig. 1. Schematic representation of the two simulation boxes, (a) MD on the left and (b) DD on the right.

2.2.3. DD simulation box and mechanical loading

The size of the simulation box is identical to the box used for MD simulation (see Fig. 1). Periodic boundary conditions are applied along the x and y directions, whereas along the z directions impenetrable surfaces are used. The loading is also consistent with the one applied to the MD box, even though the continuum-based framework of DD simulations differs fundamentally from the discrete nature of MD simulations. As a matter of fact, in the absence of bottom and top regions in DD simulations, the applied shear rate ($\dot{\gamma}_{xz}^{\mathrm{DD}}$) had to be slightly rescaled with respect to MD simulations in order to ensure the same average dislocation velocity $v = 29.8\,\mathrm{m\,s^{-1}}$. It is therefore defined as:

$$\dot{\gamma}_{xz}^{\mathrm{DD}} = \frac{L'_z}{L_z}\dot{\gamma}_{xz}^{\mathrm{MD}} = 0.94 \times 10^{7}\,\mathrm{s^{-1}} \tag{2}$$

This velocity is low enough so that the resulting friction stress at steady state remains small, here 2.9 MPa only, compared to the critical stress of the mechanism under investigation. The friction stress at steady state can be computed from $\tau_{xz} = B_{\mathrm{P}} v/b$, where $B_{\mathrm{P}} = 29.6$ μPa.s is the friction coefficient for the dislocation mobility law in the prismatic plane [24].

Although most of the DD simulations were conducted with $L_y =$ 36.7 nm and $L_z = 28$ nm, as for MD simulations, these sizes had to be adapted to explore the case of large loop sizes (large D) or lower loop densities (large L_x). In these situations, the shear strain rate was also modified in order to keep the same dislocation velocity v, using the following formula :

$$\dot{\gamma}_{xz}^{\mathrm{DD}} = \frac{vb}{L_y L_z}$$

However, it must be pointed out that this is only true for the steady state regime. It can indeed be shown that for a single dislocation gliding in the box, there is a transient regime during the loading with constant shear strain rate, because of the elasto-visco-plastic response of the box. This transient regime can be expressed as:

$$\tau_{xz}(t) = \frac{\dot{\gamma}_{xz}^{\mathrm{DD}}\, B_{\mathrm{P}} L_y L_z}{b^2}\left(1 - e^{-\frac{t\mu b^2}{B_{\mathrm{P}} L_y L_z}}\right)$$

The parameter μ is the shear modulus for the dislocations gliding in the prismatic and in the basal planes obtained by the procedure proposed in [36]. It is equal to $\mu = 36.3$ GPa [24]. It can be noticed that the transient depends on the box dimensions. This shows that even though the dimensions of the box have been adapted to keep the same dislocation velocity (at steady state), it is essential to compare the simulations with different box dimensions only when the steady state is reached. This is achieved for a simulation time higher than the characteristic time ($B_{\mathrm{P}} L_y L_z/(\mu b^2)$). In our case, this characteristic time is equal to 0.008 ns and the typical simulation time is 1.6 ns (see Fig. 4). The time step is chosen as 1×10^{-5} ns leading to 160,000 time steps for the complete simulation.

2.3. Parametric study of the effect of loop size and loop density

The influence of the loop size, given by the number of SIAs (n) or by the equivalent diameter D, has been systematically studied using MD simulation going from 4 SIAs (0.61 nm) up to 400 SIAs (6.07 nm). The effect of the box size L_x, which is related to the loop density, has also been systematically studied by MD simulation going from a box size of $L_x = 27$ nm to $L_x = 90$ nm. These 45 configurations are shown on Fig. 2 as blue filled triangles and orange filled squares.

The configurations depicted as orange filled squares have been reproduced by DD simulations. Finally, other configurations with L_x up to 200 nm and D up to 20 nm, shown as filled black circles, have been simulated to extrapolate to large loop size and lower loop density (Fig. 2).

After in-reactor operation, typical loop densities are found to be between 0.8 and 5×10^{22} m^{-3}, with loop diameters ranging from 8 to 10 nm [3]. A typical intermediate annealing leads to a loop density below 5×10^{21} m^{-3} and loop diameter between 10 and 20 nm. For long-term and high-temperature annealing, the loop density is below 1×10^{21} m^{-3} with typical loop diameters close to and larger than 20 nm.

2.4. Computation workflow

Similar to our previous study [24], special attention was given to build consistent configurations for both molecular dynamics and dislocation dynamics simulations. As such, a dedicated workflow was built using AiiDA as the workflow manager [37]. This approach allows to reproduce the entire simulation sequence, run the calculations on various computational platforms, reduce the risk of error and share the method with the scientific community. Specifically, the workflow is built from a unique set of input parameters for the DD simulation, automatically generating the corresponding MD simulation. Taking advantage of NUMODIS's crystallographic tools, the initial atomic arrangement is then built by the DD code and passed to the LAMMPS code, therefore ensuring consistency in terms of geometry, crystallography and boundary conditions. After a subsequent equilibration at 300 K over a period of 50 ps, the LAMMPS input script is automatically generated through the workflow based on the same initial NUMODIS script. Both MD and DD simulations are thereafter run on available computational facilities. The corresponding workflow has been made available as supplementary material, It can be found on the DIAMOND website [38].

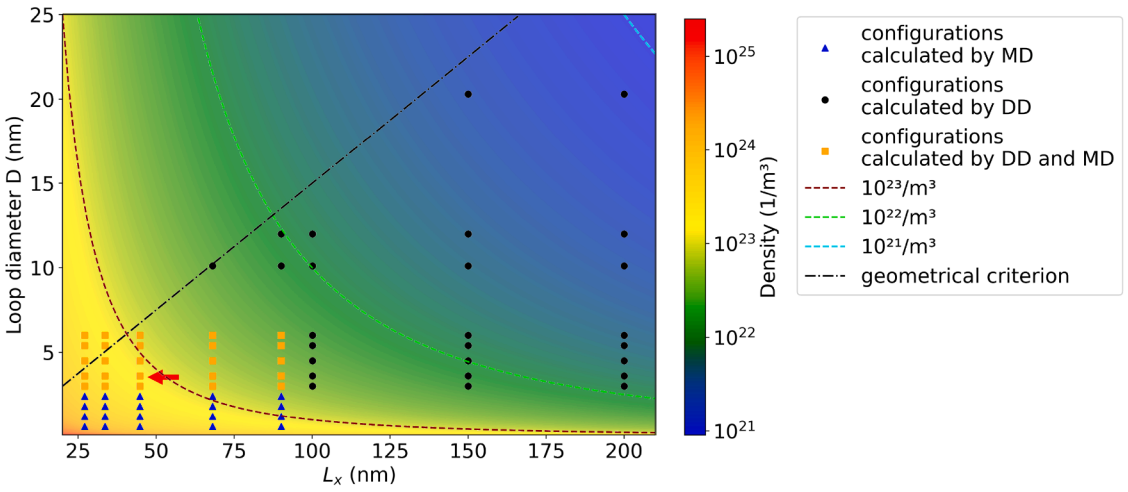

Fig. 2. Representation of each simulated configuration in a L_x - D map. The orange squares represent the configurations that have been simulated by both DD and MD. The blue triangles are the configurations that have been simulated by MD only. The black circles are the configurations that have been simulated by DD only. The background colours indicate the associated loop density N. Three isometric curves serve as a reference. The geometric limit ($D = 15\%L_x$) is plotted as a dotted line. The configuration presented in Fig. 3 and Fig. 4 is shown by the red arrow. (For interpretation of the references to colour in this figure legend, the reader is referred to the web version of this article.)

3. Results

3.1. MD simulation results

3.1.1. MD reference simulation

A reference MD simulation, with $L_x = 45$ nm and $D = 3.65$ nm (144 SIA) is first described in details. The MD sequence is shown on Fig. 3. A common-neighbor analysis with a 3.9 Å cutoff has been used to identify atoms in the core of the dislocation and of the loop. This is shown as blue atoms on Fig. 3. The evolution of the resulting shear stress τ_{xz} is plotted in Fig. 4. In addition, a schematic showing in more details the sequence, with detailed naming of the segments, is given in Fig. 5.

The screw dislocation glides in the prismatic plane and interacts with a loop that has the same Burgers vector as the dislocation. The applied strain rate ($\dot{\gamma}_{xz}$) first causes the screw dislocation P_1 to move towards the loop (Fig. 3a). Due to the long-range attractive interaction between the dislocation and the loop, the dislocation glides faster than the steady state dislocation velocity, thus explaining the negative value of the shear stress (τ_{xz}) (Fig. 4b). Then, the dislocation enters in contact with the loop on the closest basal segment B_2, which is rapidly divided into two smaller basal segments (B_2), creating an helical turn (Fig. 3b and 5b). At that point, the stress stops decreasing (Fig. 4b). The basal segments and the prismatic segments, that constitute the helical turn, then move on their glide plane leading to the expansion of the helical turn on its glide cylinder, in order to decrease the line length and thus the total energy. The two small basal segments B_2 then move away from the initial contact point on either sides, until they meet again due to the periodic boundary conditions (Fig. 5c). We note that the initial prismatic screw dislocation P_1 completely disappears as the basal segments B_2 merge again. (Fig. 3c and 5d). During these stages, the stress increases linearly (Fig. 4c).

The basal segment B_1 of the loop, which was not divided by the dislocation, progressively tilts toward its screw configuration leading to its progressive elongation (Fig. 3c), under the combined effects of the helical turn expansion and of the applied stress on its prismatic neighbor segments P_2 and P_3 (Fig. 5c).

When this basal dislocation B_1 is close enough to the screw orientation, cross-slip occurs creating a new segment in the prismatic plane P_X (Fig. 3d and 5d). It should be noted that the prismatic segment P_X that appears does not necessarily coincide with the gliding plane of the original screw dislocation.

Under the applied shear stress, the new prismatic segment P_X bows out, pushing the two basal segments B_1 sideways (Fig. 3d) and extends in both directions (Fig. 3e and 5e). The glide of the prismatic segment P_X leads to a discontinuity in the stress evolution (Fig. 4d'), because of the resulting plastic deformation. From this point onward, slight fluctuations in the stress curve can be seen. These fluctuations arise from both the glide of the P_X dislocation and the inherent stochastic nature of the MD simulation. The stress continues to increase until it reaches a critical value (Fig. 4e) at which the helical turn spontaneously closes, via an Orowan-like process, leading to a sharp drop in the stress evolution. This occurs by the merging of both sides of the P_X segment due to periodic boundary conditions. The closure occurs exactly when the P_X segment meets itself due to periodic boundary conditions and the two B_1 segments merge at points α_1 and α_2 (Fig. 5e). Finally, this leaves the original loop behind unchanged (Fig. 3f and 4f).

3.1.2. Systematic analysis of all the interactions

The evolution of stress (τ_{xz}) as function of the shear strain (γ_{xz}) was recorded for all the MD simulations. Fig. 7 shows the loading curves for the smallest box size (27 nm) and for the largest box size (90 nm).

Concerning the box with length $L_x = 27$ nm, the same stress evolution as the one shown for the reference simulation on Fig. 4 is observed for loops from 0.61 nm to 3.65 nm. However, for the three largest loops, from 4.56 nm to 6.07 nm, a linear behavior is observed without the slope discontinuity (Fig. 4d). A careful examination of the corresponding atomistic configuration, reveals that cross-slip only occurs as the applied stress peaks shortly before the closing of the helical turn. The reason for this specific behavior can be explained by the large size of the loop as compared to the box size. As a matter of fact, at zero stress, the angle of the basal segment B_1 with respect to the screw direction increases with the ratio D/L_x, therefore making cross-slip more difficult. An increase in the D/L_x ratio corresponds to an increase in loop density or an increase in loop size. Concerning the box with $L_x = 90$ nm, the same behaviour as the one seen for the reference simulation is also observed for small loops, with size between 0.61 nm to 1.83 nm. However, for loop size larger or equal than 2.43 nm a primary peak appears followed by a small stress drop, then followed by a new increase up to the maximum stress. On these last simulations, cross-slip occurs at low stress due to the small D/L_x ratio. However, a detailed investigation shows that multiple cross-slip events can occur on the basal segment B_1 leading to the formation of several new P_X segments in different parallel

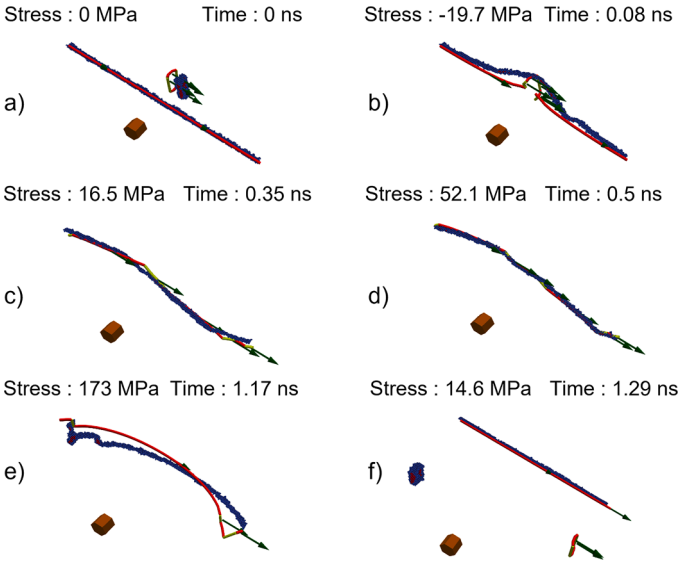

Fig. 3. Interaction between a screw dislocation gliding in its prismatic plane with a $\langle a \rangle$ loop with the same Burgers vector. The MD simulation is shown by the small blue spheres while the DD simulation corresponds to the thick line. The lines in the prismatic plane are shown in red and the lines in the basal plane are shown in yellow. The arrows indicate the direction of the Burgers vector. The crystal orientation is shown by the small hexagonal prism. (For interpretation of the references to colour in this figure legend, the reader is referred to the web version of this article.)

prismatic planes. At small and medium stress levels, the bowing of these new prismatic segments remains small, causing a competition with each other (Fig. 6a). As stress keeps increasing (combined with the effect of thermal fluctuations in MD simulations), one P_X segment is eventually favoured at the expense of the others (Fig. 6b), causing the observed stress drop. From this point, the stress increases again, until it reaches the stress required to close the helical turn.

The maximum stress, or critical stress, values (τ_c, shown as arrows on Fig. 7) for all box and loop sizes have been plotted on Fig. 8. It can be seen that a consistent trend is obtained for all the points except for the five configurations with the largest loop size and smallest box size. For these five points the maximum stress deviates from the trend observed. These five points correspond to the case where the limiting mechanism is cross-slip rather than the closing of the helical turn. These two mechanisms have clearly different evolution with box and loop sizes. As the aim of our study is to investigate the closing of the helical turn, we decided to exclude these five points from the following analysis.

Following the previous discussion, a geometrical criterion for the ratio between the loop size and box size, such as $D/L_x \leq 15\%$, is proposed to avoid this situation: below this value, the maximum stress corresponds to the closing of the helical turn as an Orowan-like process, while cross-slip is the limiting factor above this value. This criterion has been plotted as a dotted line on Fig. 2. Although the value taken here is specific to the material investigated, we expect that such criterion reflecting a geometrical effect exists in all materials.

The maximum stress values obtained from all MD simulations (without the five excluded points) have also been plotted as a function of the box size L_x on Fig. 9 as small filled circles. These maximum stresses always correspond to the closing of the helical turn. It can be seen that the larger the loop size, the higher the maximum stress. Furthermore, it is observed that the smaller the box size, the greater the maximum stress. This result is the expected size effect resulting from the bowing of the dislocation between pinning points. A detailed analysis is presented in the following.

3.2. DD simulations results

3.2.1. DD simulations of MD configurations

First, 25 configurations, previously simulated by MD, were reproduced by DD. The loop size ranged between 3.04 nm up to 6.07 nm and the box size ranged between 27 nm to 90 nm. The smallest loop sizes, from 0.61 nm to 2.43 nm, could not be reproduced by DD in order to keep a physical meaning for the length of the discretization segments. For each simulation, cross-slip occurs as in the MD simulations.

Although, there are some differences in the number of segments performing cross-slip, because of the deterministic algorithm of DD simulation, the overall dynamic is well reproduced. Fig. 3 shows for instance the detailed comparison between MD and DD simulation for a box size of 45 nm and loop size of 3.65 nm.

It is also interesting to note that the configurations with the smallest loops in the largest boxes (small D/L_x ratio) show some slight differences compared to MD, on the intermediate steps of the process (Fig. 4c to d') without any impact on the maximum stress value. In these DD simulations, the cross-slip occurs at low stress, but as the segment P_X remains too small and does not not expand, the prismatic segment (P_1) is instead activated and allows the helical turn to close. This eventually leads to the same final process: a prismatic segment is progressively activated and closes the helical turn.

All the maximum stress values obtained by DD are plotted on Fig. 9 as empty squares. It can be seen that a very good agreement is obtained between DD and MD values with a standard deviation of 4.8 MPa and a Pearson correlation coefficient equal to 0.997. This shows that the DD simulations, with all the relevant ingredients introduced, are able to predict very well the MD simulations.

3.2.2. DD simulations for extrapolation to larger size and larger box

DD simulations have then been used to predict the hardening for large loop size (D), up to 20 nm, and large box size (L_x), up to 200 nm. 26 new configurations were then investigated, while making sure that the geometrical criterion was always satisfied. For these new configurations, the box size along L_y was also increased and the shear strain rate was adapted accordingly. For instance, for a box size with $L_y = 60$ nm, the applied shear strain rate is 0.57×10^7 s^{-1}. All the maximum stresses are then recorded, making sure that the steady state is reached. These new values are shown on Fig. 9 as empty squares.

3.3. Analytical hardening model

The critical stress required to overcome one obstacle as computed by MD or DD simulations is often interpreted within the classical line tension model:

$$\tau_c = \alpha \frac{\mu b}{L_x}$$

where α is the strength coefficient of the obstacle. As part of a multiscale approach, this strength coefficient can thereafter be transferred to mesoscopic models to compute the hardening of a random population of obstacle [39–43]. Such an analysis nevertheless fails as it does not capture the effect of the loop size D on its strength.

Several authors have developed models to account for the size effect for a dislocation interacting with one precipitate through the Orowan process. In particular, Bacon, Kocks and Scattergood (BKS) [44] have proposed a model for spherical precipitates that heuristically accounts for the dislocation elastic self-interaction as it bends around this obstacle. The diameter of the precipitate is therefore introduced in the critical stress through a logarithmic term:

$$\tau_c^{\mathrm{BKS}} = \frac{\mu b}{2\pi(1-\nu_{\mathrm{P}})L} A\left(ln\left(\frac{\bar{D}}{b}\right) + B\right)$$

where $L = L_x - D$ is the inner precipitate spacing and $\bar{D} = (DL)/(D + L)$ is the harmonic average of D and L. A Poisson ratio $\nu_{\mathrm{P}} = 0.223$ has been found for dislocations gliding in the prismatic plane [24]. It must

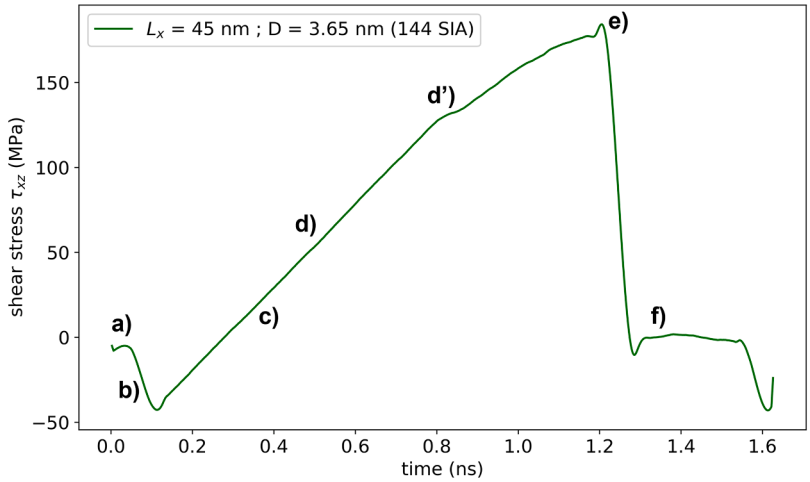

Fig. 4. Evolution of the stress over time during the MD simulation shown Fig. 3. Positions a) to f) correspond to the numbering in Fig. 3. L_x corresponds to the box length and D to the equivalent loop diameter. The number of associated SIA is recalled.

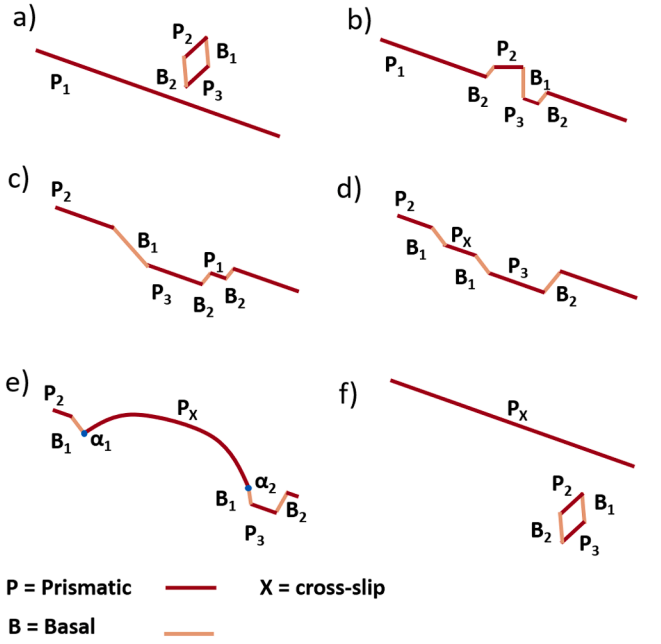

Fig. 5. Schematic showing the details of the interaction process with segment labels.

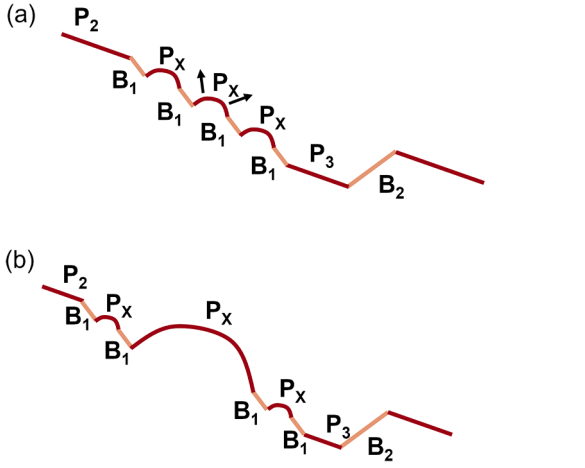

Fig. 6. Competing effect of multiple cross-slip events on the basal part of the helical turn. (a) Several cross-slip events from the basal B_1 line to different P_x prismatic planes can occur simultaneously for large box sizes. The bowing out of each of this prismatic segment is therefore limited due to their mutual competition. (b) Due to thermal fluctuations and under the applied stress, one of this P_x segment eventually expands at the expense of the others.

also be pointed out that in the original model, the parameter A is equal to 1.

More recently, Szajewksi, Crone and Knap (SCK) [45] revisited this work on stronger theoretical ground, resulting in a similar equation for spherical precipitates. Their study also indicate that the precipitate ellipticity contributes minimally to the critical stress, while the inner precipitate spacing (L) and precipitate diameter (D) play the most significant role.

Considering that the closing of an helical turn is similar to an Orowan process, the BKS model has been adjusted on our data, under the hypothesis that the loop diameter D is identical to the precipitate diameter. The two coefficients A and B of this model have been adjusted on all the values of the maximum stress deduced from MD simulations. It must be pointed out that this approach is similar to the work of Rodney [16] for the case of a screw dislocation interacting with a Frank loop in nickel. We found the following values $A = 1.23$ and $B = 0.2$, with a standard deviation of 4.2 MPa and a Pearson correlation coefficient of 0.998.

The prediction of the model is plotted on Fig. 9 as continuous colored lines. This model is then compared to all the values obtained from DD simulations, yielding and a standard deviation of 4.5 MPa and a Pearson correlation coefficient of 0.997. This shows that this simple analytical model can capture the hardening induced by small and large loops, as well as small and large loop interspacing.

4. Discussion

The stress required to close an helical turn has been investigated for a wide variety of loop size D and box size L_x using a combination of MD and DD simulations. The formation of helical turn has been observed in previous studies using the same methods in a rather wide range of materials, including nickel [16], iron [19,20], UO_2 [46] or zirconium [23]. The details of the interaction depend on the material as it involves the motion of a screw dislocation which can involve thermally activated glide or cross-slip events. A common feature of all these studies is that the critical stress for the closing of the helical turn is high and leads to significant hardening. An other feature is that the closing is similar to the Orowan process, and as such, is essentially an athermal mechanism.

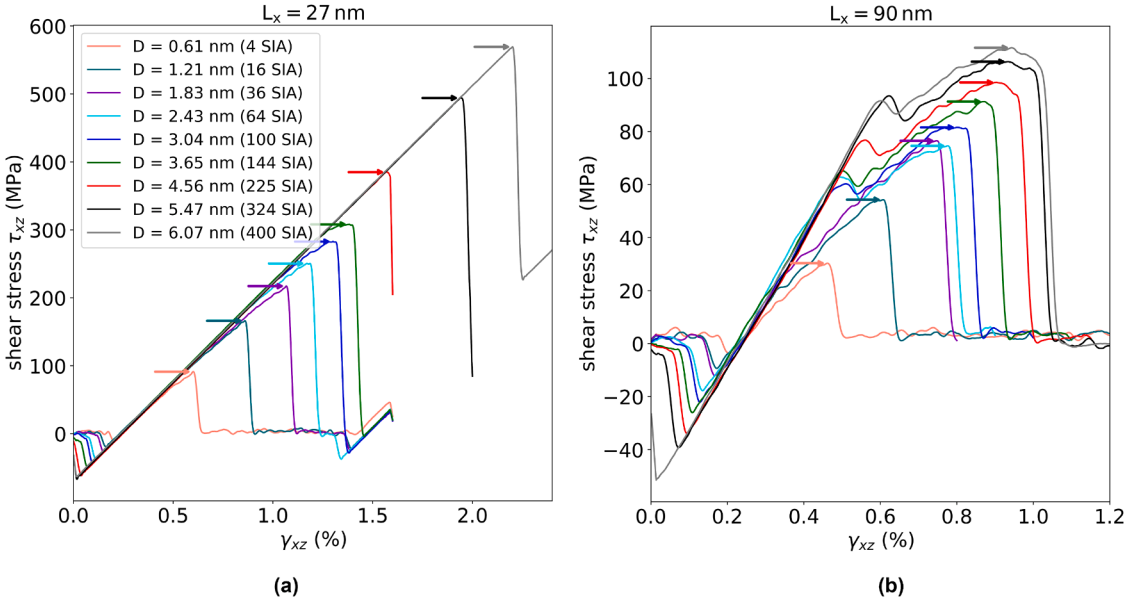

Fig. 7. Evolution of stress as a function of shear strain for each loop size and for two box sizes only, (a) $L_x = 27$ nm (left) and (b) $L_x = 90$ nm (right), in MD simulations. The maximum stresses are shown by arrows.

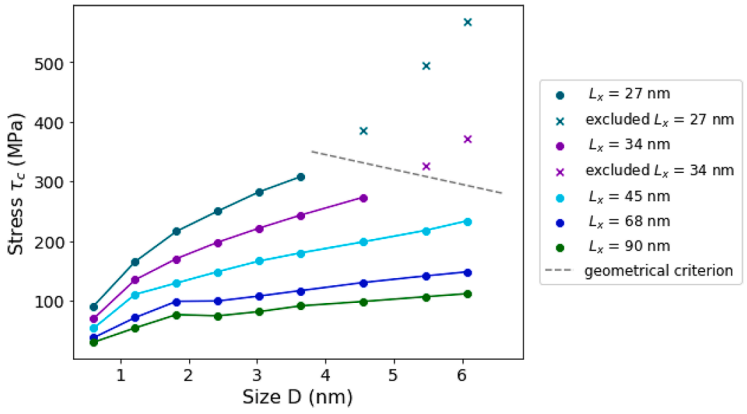

Fig. 8. Evolution of the maximum stress (τ_c) for each box size (L_x) as a function of loop size (D).

Our MD simulations have first shown that the stress required to close the helical turn decreases as the box size L_x increases. This effect had been already reported by Rodney [16]. The critical stress τ_c evolves as the inverse of the box size. This can be easily explained by the increase of the critical curvature radius (R) when L_x increases leading to the decrease of the critical stress ($\mu b/R$) according to classical dislocation theory.

Our MD simulations have also shown that the stress required to close the helical turn decreases as the loop size D decreases. Such a dependency had been reported in nickel [16] and iron [19,20]. Our results suggest that it is similar to the Orowan process for precipitates. It can be explained by the attractive interaction between the two dislocation lines on each side of the helical turn, which increases as the loop size decreases. This interaction adds up to the Peach-Koehler force due to the applied stress, and therefore reducing the stress required to close the helical turn.

It is also noteworthy that helical turns form, expand and close for square loops as small as 16 SIA ($D = 1.21$ nm) or even 4 SIA ($D = 0.61$ nm). Despite these very small sizes, the interaction mechanism described previously still occurs and the associated hardening, although lower than for larger loops, is not negligible. This result may have important implications as irradiation induces very high densities of small point defect clusters which could significantly contribute to the macroscopic hardening.

Concerning DD simulations, the remarkable agreement with MD results demonstrates that the relevant parameters, including elasticity, line energy and cross-slip, have been accurately captured by our DD model. The main differences come from the stochastic character of the MD simulations compared to the deterministic DD simulations.

The analytical model proposed exhibits a complex evolution with the box size, including a logarithmic term, that fits very well the MD and DD data over a large range of L_x values. This evolution is consistent with the evolution classically observed for Frank-Read source [41] or in the case of precipitates [44].

The analytical model also describes surprisingly well the hardening for a wide range of loop sizes, even though the original BKS model [44] was designed for precipitates and not dislocation loops. There are several reasons for this good agreement. First, due to the periodic boundary conditions, the loop, or the helical turn, remains within the small simulation box although it can be pushed away from its original location. This configuration behaves like a nearly regular square lattice, thus explaining the good agreement with the BKS model. Second, although strain fields around loops and precipitates are different, they play only a minor role in contact interactions. It is noteworthy that the size of the

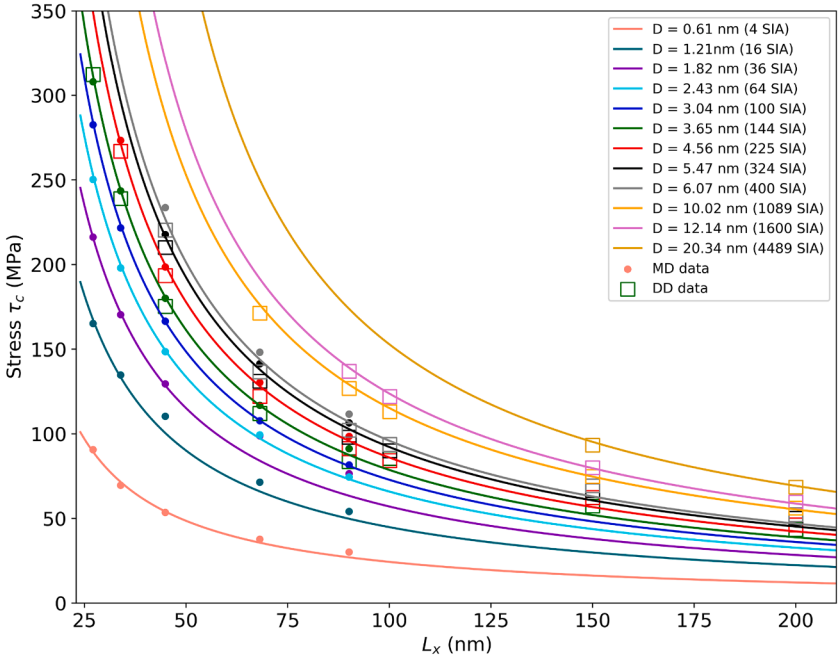

Fig. 9. Evolution of the maximum stress for each loop size (D) as a function of box size (L_x). The MD results are shown by filled circles and the DD results are shown by empty squares. The continuous lines correspond to the analytical model.

precipitate can be adequately replaced by the diameter of the loop in this model, although the loop is originally only one Burgers thick. Careful examination of the dislocation configuration as the applied shear stress peaks (Fig. 10) shows that the effective size of the helical turn is indeed close and proportional to the loop size D.

The heuristic BKS model was found to be a good approximation of an analytical model derived from theoretical basis by Szajewksi, Crone and Knap (SCK) [45] for dislocation and precipitate interaction. This SCK model should also be partly applicable to dislocation and loop interaction thus justifying theoretically the validity of the heuristic BKS model used here.

In the original BKS model the parameter A is taken as $A = 1$ [44]. Here it was chosen to adjust this parameter to $A = 1.23$. This can be justified by the anisotropic elasticity of α-Zr in MD simulations. This anisotropic elasticity is taken into account in the analytical model, and in DD simulations, by using the method proposed by Scattergood and Bacon [36]. Effective shear modulus μ and Poisson ratio ν_P are used, providing accurate description of this anisotropy for segments gliding in the prismatic planes, especially in the case of precipitates. However, because in the helical turn, there are several other segments that glide, and interact, in the basal plane (Fig. 10), the effect of the anistropic elasticity on this segments is not taken into account by the original model. The effective Poisson coefficient for segments in the basal plane is $\nu_B = 0.365$ [24]. This value is higher than the value for the prismatic plane $\nu_P = 0.223$ that is used for the analytical model. This could explain that a value for A higher than 1.0 is more suitable to account for the contribution of these basal segments.

It is interesting to note that Rodney [16] also used the BKS model to capture the loop size effect for the closing an helical turn. In his study, Rodney chose to adjust an effective diameter ($D_{\text{eff}} = CD$, with C being an adjustable parameter) for the loop while keeping the coefficient $A = 1$. Applying the same approach on our data, yields $B = -0.15$ as well as an effective loop diameter equal to $D_{\text{eff}} = 2.0D$, the later being consistent with our data as seen on Fig. 10. The associated standard deviation is then 6.9 MPa with a Pearson correlation coefficient of 0.992, both values being less satisfactory than our previous adjustment. We mention that numerical fits were also performed with the SCK model instead of the original BKS model, without providing statistically meaningful differences.

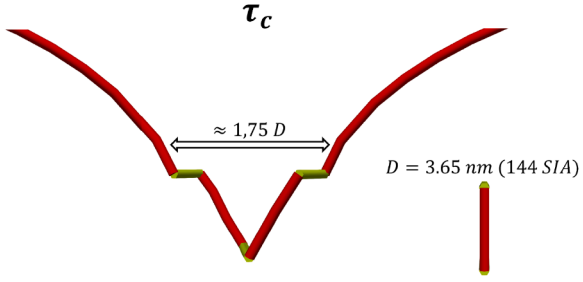

Fig. 10. Comparison between the size of the helical turn and the size of the loop at the maximum stress before closing. The size of the helical turn is correlated with the size of the loops by a factor between 1.5 and 2.0 (here 1.7).

This study has been conducted with a single loop in the simulation box. If a random array of strong fixed obstacles is considered, a correction factor close to 0.8 must be applied to the analytical model [41,47]. However, because $\langle a \rangle$ loops can glide on their cylinder, the results of the simulations may be very different when more complex configurations, for instance with mixed dislocation [30], and several loops [48,49], are considered. In that case, loops and helical turns can glide on their cylinder and rearrange resulting in very different outcomes. Further studies are needed in order to evaluate the impact of the collective loop rearrangement on the resulting hardening.

5. Conclusion

Molecular dynamics simulations were carried out on pure zirconium at 300K to study the effect of loop size and density on the resulting hardening. A specific configuration was studied where a screw dislocation interacts with a loop that has the same Burgers vector as the dislocation. This interaction leads to the formation of an helical turn. It was shown that the maximum stress needed to overcome the obstacle and close the helical turn decreases as the box size increases, in good agreement with

classical dislocation theory. On the other hand the maximum stress increases as the loop size increases. This can be explained by the attractive interaction between the two dislocation lines on each side of the helical turn. Extending the conclusions of this study to higher temperatures would require several additional MD simulations at various temperatures in order to verify that the temperature does not significantly alter the mechanisms involved.

The very same configurations have been simulated by discrete dislocation dynamics simulations. Excellent agreements are obtained between DD and MD simulations showing that the relevant parameters introduced, including elasticity, line energy and cross-slip, are accurately captured by our DD model. Quantitatively, a standard deviation of only 4.8 MPa and a correlation coefficient of 0.997 are obtained between the two types of simulations within their overlapping calculation ranges. Thanks to this excellent agreement, DD simulations have been used to extrapolate the results to larger loop sizes, up to diameter of 10 nm, and larger box sizes, up to 100 nm.

An analytical hardening model, based on the BKS model, has then been adjusted on the obtained maximum stresses. Although this model was originally designed for dislocation and precipitate interaction, it is able to describe very accurately the hardening induced by loops in a wide range of loop size and box size. Provided that loop size and density are known, this analytical model could be used to predict the irradiation induced hardening of zirconium and its evolution during post-irradiation annealing. Further works are still needed to investigate the effect of the loop mobility on the resulting hardening.

CRediT authorship contribution statement

P. Noirot: Writing – review & editing, Writing – original draft, Visualization, Validation, Methodology, Investigation, Data curation; **L. M. Dupuy:** Writing – review & editing, Writing – original draft, Visualization, Supervision, Software, Resources, Methodology, Investigation, Data curation, Conceptualization; **J. Daubin:** Software; **F. Mompiou:** Writing – review & editing, Writing – original draft, Supervision, Conceptualization; **F. Onimus:** Writing – review & editing, Writing – original draft, Supervision, Methodology, Funding acquisition, Conceptualization.

Data availability

Data will be made available on request.

Declaration of competing interest

The authors declare that they have no known competing financial interests or personal relationships that could have appeared to influence the work reported in this paper.

Acknowledgments

This work has been funded by the Project PRECCI from the French nuclear tripartite institute CEA EDF Framatome. L.D. acknowledges the continuous support of the MATIX project for the development of the NUMODIS code. This work has been partially supported by the project DIAMOND (ANR-22-PEXD-0015) of the PEPR DIADEM (ANR-22-PEXD-0001).

References

[1] F. Onimus, S. Doriot, J.L. Béchade, et al., Radiation effects in zirconium alloys, in: Comprehensive Nuclear Materials, Elsevier, 2020, pp. 1–56. https://doi.org/10.1016/B978-0-12-803581-8.11759-X

[2] A. Jostsons, P.M. Kelly, R.G. Blake, The nature of dislocation loops in neutron irradiated zirconium, J. Nucl. Mater. 66 (3) (1977) 236–256. https://doi.org/10.1016/0022-3115(77)90113-1

[3] D.O. Northwood, R.W. Gilbert, L.E. Bahen, P.M. Kelly, R.G. Blake, A. Jostsons, P.K. Madden, D. Faulkner, W. Bell, R.B. Adamson, et al., Characterization of neutron irradiation damage in zirconium alloys - an international "round-robin" experiment, J. Nucl. Mater. 79 (2) (1979-02) 379–394. https://doi.org/10.1016/0022-3115(79)90103-X

[4] M. Griffiths, A review of microstructure evolution in zirconium alloys during irradiation, J. Nucl. Mater. 159 (1988-10) 190–218. https://doi.org/10.1016/0022-3115(88)90093-1

[5] P.M. Kelly, R.G. Blake, The characterization of dislocation loops in neutron irradiated zirconium, Philos. Mag. 28 (2) (1973-08) 415–426. https://doi.org/10.1080/14786437308217463

[6] D.O. Northwood, A.R. Causey, Microstructural changes during thermally induced strain recovery in irradiated zircaloy-4 stress relaxation specimens, J. Nucl. Mater. 64 (3) (1977-02) 308–312. https://doi.org/10.1016/0022-3115(77)90084-8

[7] J. Ribis, F. Onimus, J.-L. Béchade, S. Doriot, C. Cappelaere, C. Lemaignan, A. Barbu, O. Rabouille, Experimental and modeling approach of irradiation defects recovery in zirconium alloys: impact of an applied stress, J. ASTM Int. (JAI) 5 (3) (2008) 674–695. https://doi.org/10.1520/STP48162S

[8] J. Ribis, F. Onimus, J.-L. Béchade, S. Doriot, A. Barbu, C. Cappelaere, C. Lemaignan, et al., Experimental study and numerical modelling of the irradiation damage recovery in zirconium alloys, J. Nucl. Mater. 403 (1) (2010-08) 135–146. https://doi.org/10.1016/j.jnucmat.2010.06.012

[9] B. Bourdiliau, F. Onimus, C. Cappelaere, V. Pivetaud, P. Bouffioux, V. Chabretou, A. Miquet, et al., Impact of irradiation damage recovery during transportation on the subsequent room temperature tensile behavior of irradiated zirconium alloys, J. ASTM Int., 9 7, (2010) 929–953. https://doi.org/10.1520/STP152920120037

[10] B.V. Cockeram, K.J. Leonard, T.S. Byun, L.L. Snead, J.L. Hollenbeck, et al., The recovery of irradiation damage for zircaloy-2 and zircaloy-4 following low dose neutron irradiation at nominally 358 °c, J. Nucl. Mater. 461 (2015-06) 244–264. https://doi.org/10.1016/j.jnucmat.2015.03.003

[11] F. Onimus, S. Doriot, A. Ambard, F. Bourlier, B. Verhaeghe, T. Le Jolu, C. Cappelaere, et al., Understanding post-irradiation creep behavior of M5Framatome zirconium alloy, J. Nucl. Mater. 597 (2024-08) 155138. https://doi.org/10.1016/j.jnucmat.2024.155138

[12] D.J. Bacon, Y.N. Osetsky, D. Rodney, et al., Chapter 88 dislocation-obstacle interactions at the atomic level, in: Dislocations in Solids, 15, Elsevier, 2009, pp. 1–90. https://doi.org/10.1016/S1572-4859(09)01501-0

[13] Y. Osetsky, D. Rodney, Atomic-Level Dislocation dynamics in irradiated metals, in: Comprehensive Nuclear Materials, Elsevier, 2020, Vol. 1 pp. 663–688. https://doi.org/10.1016/B978-0-12-803581-8.00662-7

[14] L. Kubin, Dislocations, Mesoscale Simulations and Plastic Flow, Oxford Series on Materials Modelling, Oxford University Press, Oxford, New York, Oxford, New York, 2013.

[15] D. Rodney, G. Martin, Dislocation pinning by glissile interstitial loops in a nickel crystal: a molecular-dynamics study, Phys. Rev. B 61 (2000) 8714–8725. https://doi.org/10.1103/PhysRevB.61.8714

[16] D. Rodney, Molecular dynamics simulation of screw dislocations interacting with interstitial frank loops in a model FCC crystal, Acta Mater. 52 (3) (2004) 607–614. https://doi.org/10.1016/j.actamat.2003.09.044

[17] T. Nogaret, C. Robertson, D. Rodney, et al., Atomic-scale plasticity in the presence of Frank loops, Philos. Mag. 87 (6) (2007-02-21) 945–966. https://doi.org/10.1080/14786430601011497

[18] D. Rodney, Atomic modeling of irradiation-induced hardening, C.R. Phys. 9 (3) (2008) 418–426. Materials subjected to fast neutron irradiation, https://doi.org/10.1016/j.crhy.2007.08.005

[19] X.-Y. Liu, S.B. Biner, Molecular dynamics simulations of the interactions between screw dislocations and self-interstitial clusters in body-centered cubic Fe, Scr. Mater. 59 (1) (2008) 51–54. https://doi.org/10.1016/j.scriptamat.2008.02.031

[20] D. Terentyev, D.J. Bacon, Y.N. Osetsky, Reactions between a 1/2⟨111⟩ screw dislocation and ⟨100⟩ interstitial dislocation loops in α-iron modelled at atomic scale, Phil. Mag. 90 (7–8) (2010) 1019–1033. https://doi.org/10.1080/14786430903019073.

[21] R.E. Voskoboynikov, Y.N. Osetsky, D.J. Bacon, Self-interstitial atom clusters as obstacles to glide of 1/3 ⟨11-20⟩ {1-100} edge dislocations in α-zirconium, Mater. Sci. Eng.: A 400–401 (2005) 54–58. Dislocations 2004, https://doi.org/10.1016/j.msea.2005.03.056

[22] R.E. Voskoboinikov, Y.N. Osetsky, D.J. Bacon, Interaction of 1/3<11-20>(0001) edge dislocation with point defect clusters created in displacement cascades in α-zirconium, Mater. Sci. Eng.: A 400–401 (2005) 49–53. Dislocations 2004, https://doi.org/10.1016/j.msea.2005.03.055

[23] A. Serra, D.J. Bacon, Atomic-level computer simulation of the interaction between 1/3 [11-20] {1-100} dislocations and 1/3 [11-20] interstitial loops in α-zirconium, Modell. Simul. Mater. Sci. Eng. 21 (4) (2013) 045007. https://doi.org/10.1088/0965-0393/21/4/045007

[24] L.M. Dupuy, W. Kassem, E. Clouet, F. Onimus, Atomistically informed dislocation dynamics simulations: application to dislocation-loop interactions in zirconium, Modell. Simul. Mater. Sci. Eng. 32 (3) (2024) 035015. https://doi.org/10.1088/1361-651X/ad278a

[25] D. Caillard, M. Rautenberg, X. Feaugas, et al., Dislocation mechanisms in a zirconium alloy in the high-temperature regime: an *in situ* TEM investigation, Acta Mater. 87 (2015-04) 283–292. https://doi.org/10.1016/j.actamat.2015.01.016

[26] D. Caillard, M. Gaumé, F. Onimus, et al., Glide and cross-slip of a-dislocations in Zr and Ti, Acta Mater. 155 (2018-08) 23–34. https://doi.org/10.1016/j.actamat.2018.05.038

[27] J. Drouet, L. Dupuy, F. Onimus, F. Mompiou, S. Perusin, A. Ambard, et al., Dislocation dynamics simulations of interactions between gliding dislocations and radiation induced prismatic loops in zirconium, J. Nucl. Mater. 449 (1) (2014-06) 252–262. https://doi.org/10.1016/j.jnucmat.2013.11.049
[28] S. Plimpton, Fast parallel algorithms for short-Range molecular dynamics, J. Comput. Phys. 117 (1) (1995) 1–19. https://doi.org/10.1006/jcph.1995.1039
[29] M.I. Mendelev, G.J. Ackland, Development of an interatomic potential for the simulation of phase transformations in zirconium, Philos. Mag. Lett. 87 (5) (2007) 349–359. https://doi.org/10.1080/09500830701191393
[30] F. Onimus, L. Dupuy, M. Gaumé, W. Kassem, F. Mompiou, et al., Deformation mechanisms of zirconium alloys after irradiation studied by dislocation dynamics simulations and in situ straining experiments in TEM, ASTM International 100 Barr Harbor Drive, PO Box C700, West Conshohocken, PA 19428-2959, 2021-07-01, pp. 319–342. https://doi.org/10.1520/STP162220190036
[31] M. Verdier, M. Fivel, I. Groma, Mesoscopic scale simulation of dislocation dynamics in fcc metals: principles and applications, Modell. Simul. Mater. Sci. Eng. 6 (6) (1998) 755. https://doi.org/10.1088/0965-0393/6/6/007
[32] B. Devincre, R. Madec, G. Monnet, S. Queyreau, R. Gatti, L. Kubin, Modeling crystal plasticity with dislocation dynamics simulations: the 'microMegas' code, Mech. Nano-objects 1 (2011) 81–100.
[33] D. Weygand, L.H. Friedman, E.V.d. Giessen, A. Needleman, Aspects of boundary-value problem solutions with three-dimensional dislocation dynamics, Modell. Simul. Mater. Sci. Eng. 10 (4) (2002) 437. https://doi.org/10.1088/0965-0393/10/4/306
[34] V.V. Bulatov, W. Cai, Computer Simulations of Dislocations, Oxford Series on Materials Modelling, Oxford University Press, Oxford, New York, Oxford, New York, 2006.
[35] A. Arsenlis, W. Cai, M. Tang, M. Rhee, T. Oppelstrup, G. Hommes, T.G. Pierce, V.V. Bulatov, Enabling strain hardening simulations with dislocation dynamics, Modell. Simul. Mater. Sci. Eng. 15 (6) (2007) 553. https://doi.org/10.1088/0965-0393/15/6/001
[36] R.O. Scattergood, D.J. Bacon, The Orowan mechanism in anisotropic crystals, Philos. Mag. 31 (770001989) (1975) 179–198. https://doi.org/10.1080/14786437508229295
[37] S.P. Huber, S. Zoupanos, M. Uhrin, L. Talirz, L. Kahle, R. Häuselmann, D. Gresch, T. Müller, A.V. Yakutovich, C.W. Andersen, et al., AiiDA 1.0, a scalable computational infrastructure for automated reproducible workflows and data provenance, Sci. Data 7 (1) (2020) 300.
[38] (https://diamond-diadem.github.io/workflows/noirot2025).
[39] J. Friedel, Les dislocations, 1956.
[40] A.K. Seeger, On the theory of radiation damage and radiation hardening, in: Proceedings of the Second United Nations International Conference on the Peaceful Uses of Atomic Energy, 6, Geneva, 1958, pp. 250–273.
[41] A.J.E. Foreman, M.J. Makin, Dislocation movement through random arrays of obstacles, Philos. Mag. 14 (131) (1966) 911–924. https://doi.org/10.1080/14786436608244762
[42] A. Argon, Strengthening mechanisms in crystal plasticity, Oxford University Press, 2007.
[43] G. Monnet, New insights into radiation hardening in face-centered cubic alloys, Scr. Mater. 100 (2015) 24–27. https://doi.org/10.1016/j.scriptamat.2014.12.003
[44] D.J. Bacon, U.F. Kocks, R.O. Scattergood, et al., The effect of dislocation self-interaction on the orowan stress, Philos. Mag. 28 (6) (1973-12) 1241–1263. https://doi.org/10.1080/14786437308227997
[45] B.A. Szajewski, J.C. Crone, J. Knap, Analytic model for the Orowan dislocation-precipitate bypass mechanism, Materialia 11 (2020) 100671. https://doi.org/10.1016/j.mtla.2020.100671
[46] M. Borde, L. Dupuy, A. Pivano, B. Michel, D. Rodney, J. Amodeo, Interaction between 1/2<110>{001} dislocations and {110} prismatic loops in uranium dioxide: implications for strain-hardening under irradiation, Int. J. Plast. 168 (2023) 103702. https://doi.org/10.1016/j.ijplas.2023.103702
[47] A. de Vaucorbeil, C.W. Sinclair, W.J. Poole, Dislocation glide through non-Randomly distributed point obstacles, Philos. Mag. 93 (27) (2013) 3664–3679. https://doi.org/10.1080/14786435.2013.820384
[48] F. Onimus, I. Monnet, J.L. Béchade, C. Prioul, P. Pilvin, et al., A statistical TEM investigation of dislocation channeling mechanism in neutron irradiated zirconium alloys, J. Nucl. Mater. 328 (2) (2004-07) 165–179. https://doi.org/10.1016/j.jnucmat.2004.04.337
[49] T. Nogaret, D. Rodney, M. Fivel, C. Robertson, et al., Clear band formation simulated by dislocation dynamics: role of helical turns and pile-ups, J. Nucl. Mater. 380 (1) (2008-10) 22–29. https://doi.org/10.1016/j.jnucmat.2008.07.001